ARTICLES
https://doi.org/10.1038/s41567-022-01541-y

nature physics

Check for updates

OPEN

Band transport by large Fröhlich polarons in MXenes

Wenhao Zheng[1], Boya Sun[2,3], Dongqi Li[2], Sai Manoj Gali[4], Heng Zhang[1], Shuai Fu[1], Lucia Di Virgilio[1], Zichao Li[5], Sheng Yang[2], Shengqiang Zhou[5], David Beljonne[4], Minghao Yu[2], Xinliang Feng[2,6], Hai I. Wang[1]✉ and Mischa Bonn[1]✉

MXenes are emerging layered materials that are promising for electrochemical energy storage and (opto-)electronic applications. A fundamental understanding of charge transport in MXenes is essential for such applications, but has remained under debate. While theoretical studies pointed to efficient band transport, device measurements have revealed thermally activated, hopping-type transport. Here we present a unifying picture of charge transport in two model MXenes by combining ultrafast terahertz and static electrical transport measurements to distinguish the short- and long-range transport characteristics. We find that band-like transport dominates short-range, intra-flake charge conduction in MXenes, whereas long-range, inter-flake transport occurs through thermally activated hopping, and limits charge percolation across the MXene flakes. Our analysis of the intra-flake charge carrier scattering rate shows that it is dominated by scattering from longitudinal optical phonons with a small coupling constant ($\alpha \approx 1$), for both semiconducting and metallic MXenes. This indicates the formation of large polarons in MXenes. Our work therefore provides insight into the polaronic nature of free charges in MXenes, and unveils intra- and inter-flake transport mechanisms in the MXene materials, which are relevant for both fundamental studies and applications.

Two-dimensional (2D) transition metal carbides and/or nitrides, known as MXenes, have attracted considerable attention as a consequence of their outstanding electronic, optical, mechanical and thermal properties[1–3]. The general formula of MXenes is $M_{n+1}X_nT_x$ ($n = 1$–4), where M represents the transition metal, X carbon and/or nitrogen and T_x the surface termination. A unique combination of tunable electronic properties (through the $M_{n+1}X_n$ backbone) and versatile surface chemistry (from T_x functionalization) results in many intriguing properties such as the metal-to-insulator transition, topological insulators and superconductivity[4]. As such, MXenes hold great promise for a variety of electronic and optoelectronic applications[1–3].

In many applications, the electrical transport properties of MXenes are quintessential. Understanding the mechanism governing the electrical conductivity of MXenes is therefore important. Accordingly, many previous studies have investigated the conductivity of charge carriers, specifically as a function of temperature (T). However, controversial results, mainly between experiments and theoretical calculations, have been reported. Experimentally[5–8], based on static electrical transport studies using four-probe methods, it has been shown that the conductivity σ increases at elevated temperature T (that is, $d\sigma/dT > 0$). This dependence was attributed to a thermally activated hopping transport. On the other hand, theoretical studies have predicted band-like transport[9–11]. For band transport, the charge carrier mobility typically increases with decreasing T (that is, $d\sigma/dT < 0$) as a result of the decreased carrier–phonon scattering probability at lower T. This contradiction between the theoretical and experimental results raises questions regarding the nature of the charge carriers and charge transport mechanism in MXenes. Owing to the polar nature of MXene crystals[3], charge carriers can induce lattice distortions via Coulomb interactions. A quasi-particle, a so-called polaron, is normally introduced to describe the charge carriers dressed with lattice distortions. The carrier–phonon coupling constant α characterizes the strength of the coupling between charge carriers and phonons[12]. For sufficiently strong carrier–phonon coupling ($\alpha \gg 6$), self-trapped, localized polaron states, or so-called small polarons (with the lattice distortion limited to ~1 lattice unit), occur. Transport of small polarons requires thermal activation, which may explain the observed hopping-like transport behaviour in MXenes. For weaker coupling ($\alpha < 6$), large polarons are formed; these are characterized by band-like transport of charge carriers with a renormalized effective mass. Large polaron mobility typically increases with decreasing temperature[12,13]. We note that other charge localization effects, for example, due to the presence of a high density of defects (depending on the quality of the samples), could lead to hopping-like transport as well[14]. Given the increasing interest in MXenes for electrical and electrochemical applications, it is crucial to understand the nature of charge species and their transport mechanism across materials and interfaces.

In this Article, we present a unifying picture of charge transport in liquid-exfoliated MXenes, using semiconductor-like $Nb_4C_3T_x$ and metallic $Ti_3C_2T_x$ as model systems. By comprehensively employing ultrafast terahertz and static electrical transport measurements, we distinguish the short- and long-range transport characteristics of MXene films. We reveal that while band-like transport dominates intra-flake charge conduction in MXenes, inter-flake transport occurs via thermally activated hopping processes and becomes the

[1]Max Planck Institute for Polymer Research, Mainz, Germany. [2]Center for Advancing Electronics Dresden (cfaed) & Faculty of Chemistry and Food Chemistry, Technische Universität Dresden, Dresden, Germany. [3]State Key Laboratory of Metal Matrix Composites, School of Materials Science and Engineering, Shanghai Jiao Tong University, Shanghai, China. [4]Laboratory for Chemistry of Novel Materials, Université de Mons, Mons, Belgium. [5]Institute of Ion Beam Physics and Materials Research, Helmholtz-Zentrum Dresden-Rossendorf, Dresden, Germany. [6]Max Planck Institute of Microstructure Physics, Halle, Germany. ✉e-mail: wanghai@mpip-mainz.mpg.de; bonn@mpip-mainz.mpg.de

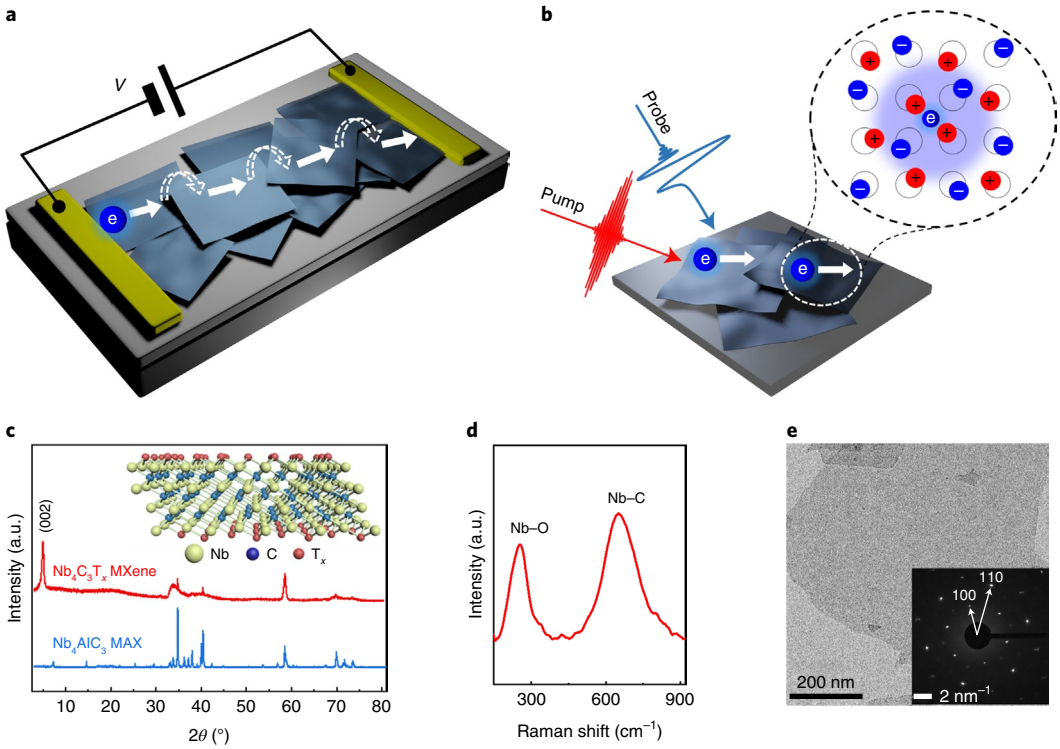

Fig. 1 | Charge transport measurement modes and characterizations of MXene samples. a, Schematic of charge transport within the network of MXene flakes. The inter-crystallite charge carrier hopping (indicated by the dashed arrows) is revealed as the charge transport bottleneck, limiting the overall charge conduction between electrodes. **b**, Scheme for ultrafast OPTP experiments to characterize the intra-MXene flake transport of charge carriers. Inset: the formation of a large polaron, in which a conduction electron is dressed by lattice deformations extending over several lattice constants. **c**, XRD spectra of Nb_4AlC_3 MAX (the mother compounds) and resultant $Nb_4C_3T_x$ after etching. Inset: the crystal structure of $Nb_4C_3T_x$ MXene. **d**, Raman spectrum of delaminated $Nb_4C_3T_x$ MXene. **e**, TEM image of $Nb_4C_3T_x$ MXene. Inset: corresponding SAED pattern, which shows the high crystallinity and hexagonal symmetry of the crystal lattice.

limiting step for charge percolation across the MXene flakes (see the illustration in Fig. 1a). More importantly, by analysing contributions from impurities, acoustic and longitudinal optical (LO) phonons to the charge scattering mechanisms, we further show that carrier–LO phonon scattering dominates the carrier transport at room T, with a small carrier–LO phonon coupling constant ($\alpha \approx 1$). The small α indicates the formation of large polarons in the materials (see the illustration in Fig. 1b). These results suggest that, for both semiconducting and metallic MXenes, large polaron formation is a generic property that fundamentally affects the intrinsic charge transport and carrier lifetime. Our results reconcile the debate between previous theoretical and experimental studies and shed light on the charge species and their transport mechanisms in MXenes.

Results and discussion

We present detailed structural characterizations for $Nb_4C_3T_x$ MXene in Fig. 1, and show those for the well-established $Ti_3C_2T_x$ MXene in Supplementary Fig. 1. Figure 1c presents the X-ray diffraction (XRD) pattern of the Nb_4AlC_3 MAX precursor and the resultant $Nb_4C_3T_x$ MXene following the selective etching of aluminium element by hydrogen fluoride. After etching, the diffraction peaks corresponding to the MAX phase either disappear or greatly diminish in intensity, along with the appearance of a new peak at a 2θ of ~5°. This new peak can be assigned to the (002) facet for $Nb_4C_3T_x$ MXene[6]. Furthermore, Raman spectroscopy displays two pronounced peaks at ~240 cm^{-1} and 675 cm^{-1}, corresponding to Nb–O and Nb–C vibrational modes, respectively (Fig. 1d). The emergence of the Nb–O peak at ~240 cm^{-1} points to (partial) surface oxidation, which is unavoidable during the synthesis process. Such surface oxidation might partially contribute to the semiconducting nature of $Nb_4C_3T_x$ MXene in our study. In other MXenes (for example, $Ti_4N_3T_x$), surface oxidation has been reported to lead to a bandgap opening, thus provoking a metal-to-semiconductor transition[15]. In addition, as shown in X-ray photoelectron spectroscopy (XPS) results, the as-synthesized $Nb_4C_3T_x$ has mixed termination (Supplementary Fig. 2 and Supplementary Discussion). High-angle annular dark-field scanning transmission electron microscopy (HAADF-STEM) and energy-dispersive X-ray analysis (EDX) display uniform distributions of Nb, C, F and O in $Nb_4C_3T_x$ MXene (Supplementary Fig. 3). A selected-area electron diffraction (SAED) pattern of a $Nb_4C_3T_x$ flake demonstrates the high crystallinity and hexagonal symmetry ($P6_3/mmc$), in line with typical MXene structures[3,6]. We further conducted high-resolution atomic force microscope (AFM) measurements, which are described in Supplementary Fig. 4. Based on the analysis, over ~60% of the MXene flakes are ~5 nm in thickness, corresponding to a bilayer structure for $Nb_4C_3T_x$ MXene[6]. The homogeneity and good quality of our samples are further confirmed by transmission electron microscopy (TEM) and scanning electron microscopy characterizations in Fig. 1e and Supplementary Fig. 5, showing that the lateral dimension is on the order of several micrometres.

Niobium-based MXene has been predicted to have a narrow bandgap (on the order of ~0.1 eV)[16]. In line with this prediction, the bandgap of $Nb_4C_3T_x$ in our study was determined to be ~0.19 eV from the Tauc plot method (Supplementary Fig. 7). Static terahertz measurements further support the narrow-gap nature of the $Nb_4C_3T_x$ MXene. We find negligible conductivity (or, equivalently, absorption) by free charge carriers in our 0–2 THz window

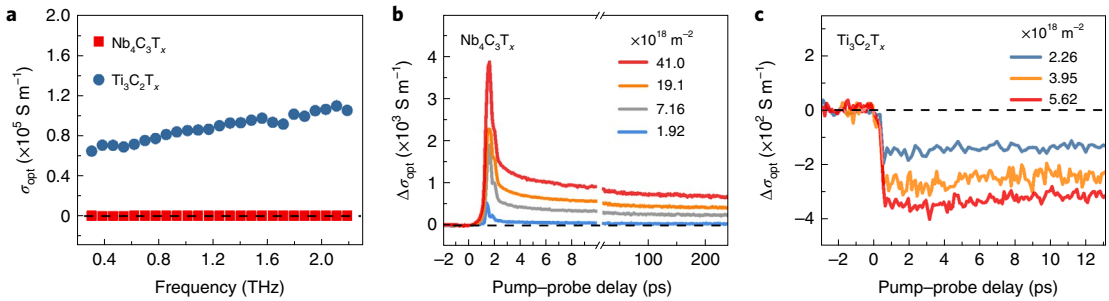

Fig. 2 | Static terahertz conductivity (absorption) and ultrafast photoconductivity of semiconducting and metallic MXene samples. a, Static terahertz conductivity of $Nb_4C_3T_x$ and $Ti_3C_2T_x$ MXene thin films. **b**,**c**, The fluence-dependent, time-resolved photoconductivity of semiconducting $Nb_4C_3T_x$ (**b**) and metallic $Ti_3C_2T_x$ (**c**) MXenes thin films, following 1.55 eV photoexcitation at room temperature.

(corresponding to 0–8 meV; Fig. 2a). In contrast, the metallic $Ti_3C_2T_x$ exhibits substantial conductivity (absorption) in this terahertz region (Fig. 2a).

The different—semiconducting and metallic—natures of $Nb_4C_3T_x$ and $Ti_3C_2T_x$ MXenes, respectively, give rise to distinct photoresponses, as shown in Fig. 2b,c. Photoexcitation of a semiconductor like $Nb_4C_3T_x$ promotes electrons to the conduction band, increasing the material's conductivity from ~0 (Fig. 2a) to a finite value (that is, giving rise to a positive photoconductivity)[17]. In contrast, for metallic materials such as $Ti_3C_2T_x$, optical excitation of conducting electrons results in heating up of the electron gas, which gives rise to a transiently reduced conductivity (that is, negative photoconductivity)[18]. The samples' photoconductivity is determined by optical-pump terahertz-probe (OPTP) spectroscopy. OPTP spectroscopy provides insight into the electrical transport properties of charge carriers in a contact-free and non-invasive fashion[17,19–21]. Thanks to the transient nature of terahertz probe pulses (with duration of ~1 ps), terahertz spectroscopy characterizes short-range, intra-flake transport (over approximately tens of nanometres) in MXenes[17,22]. By monitoring the photo-induced terahertz absorption (ΔE) at various pump–probe delays, the photoconductivity ($\Delta\sigma_{opt}$) dynamics can be quantified using the thin-film approximation as follows[17]:

$$\Delta\sigma_{opt} = -\frac{n_{sub}+1}{Z_0 L} \times \frac{E_{pump}-E_0}{E_0} \quad (1)$$

where $Z_0 = 377\,\Omega$ is the impedance of free space, $n_{sub} = 1.95$ is the refractive index of the fused-silica substrate in the terahertz range and L is the excitation thickness. E_{pump} and E_0 represent the transmitted terahertz electric field with and without photoexcitation, respectively (see Methods for details).

The photoconductivity of $Nb_4C_3T_x$ MXene (Fig. 2b) decays swiftly within several picoseconds, followed by a slow decay (>1 ns, limited by our temporal probe window). We attribute the fast photoconductivity decay in the $Nb_4C_3T_x$ MXene to the trapping of free charge carriers at defects. This claim is supported by the fluence-dependent OPTP dynamics analysis, in which trap filling is observed (Supplementary Fig. 8 and Supplementary Discussion)[23]. In addition, by comparing different sample batches, we observe that, for samples with a slightly higher degree of oxidation (characterized by Raman spectroscopy), the relative weight of the fast decay is higher (Supplementary Fig. 9). As such, surface oxidation is a potential candidate for defect formation and charge carrier trapping[15]. The negative photoconductivity in $Ti_3C_2T_x$ MXene confirms the metallic nature of $Ti_3C_2T_x$. The transient photoconductivity decrease in metallic $Ti_3C_2T_x$ MXene is consistent with previous reports[24]. Therefore, the ultrafast terahertz photoconductivity traces shown in Fig. 2 confirm the semiconductor-like behaviour in $Nb_4C_3T_x$ MXene and a metallic response in $Ti_3C_2T_x$ MXene.

To investigate the charge transport mechanism in $Nb_4C_3T_x$ MXenes, we complementarily employed temperature-dependent ultrafast OPTP and static electrical measurements. To provide a fair comparison between terahertz and electrical studies, we followed the same film deposition recipe to make thin films of $Nb_4C_3T_x$. As shown in Fig. 3a, the photoconductivity increases at reduced temperatures by a factor of 3–4, that is, $d\Delta\sigma_{opt}/dT < 0$. Meanwhile, a substantial, yet opposite trend ($d\sigma_{ele}/dT > 0$) is observed in electrically measured conductivity. The spectroscopic result suggests that band-like transport dominates the charge transport mechanism in $Nb_4C_3T_x$ MXene, with thermally populated phonons limiting the charge mobility through carrier–phonon scattering. Notably, a temperature dependence $T^{-\beta}$ of the conductivity has been predicted in molybdenum- and titanium-based MXenes, with $1.5 < \beta < 2.1$ (refs. [9,10]). Our results reveal $\beta \approx 1$ for the averaged long-lived photoconductivity (as shown in Fig. 3b). This experimentally observed weaker temperature dependence of the conductivity suggests that, besides the dominant role of phonons, impurity scattering may also contribute to the limitation of the charge transport in $Nb_4C_3T_x$ MXene.

We note that the $d\Delta\sigma_{opt}/dT < 0$ in our spectroscopic result is in line with previous theoretical studies[9–11], but in stark contrast to the $d\sigma_{ele}/dT > 0$ in device results shown here and also reported previously for other MXene materials measured using the four-probe method[5–7]. This apparent contradiction can be explained as follows. In the terahertz photoconductivity measurements, the transient, picosecond-duration terahertz field drives the charge carrier over approximately tens of nanometres. Therefore, terahertz spectroscopy provides the local, intra-flake charge transport information (given the micrometre size of the flakes). Meanwhile, static electrical transport studies provide long-range charge carrier conductance over macroscopic distances between the electrodes under d.c. bias[14,25]. As such, we can rationalize the results by postulating band-like transport dominating intra-flake charge conduction, while the inter-flake hopping is the rate-limiting step for charge percolation through devices consisting of many MXene flakes. Importantly, such a scenario reconciles the debate between previous theoretical and experimental studies on the charge transport mechanism in MXenes. Moreover, these findings are relevant for the optimization of MXene-based devices: for example, interface molecular engineering to enhance the inter-flake transport or increasing the geometrical size is therefore recommended[26].

To further confirm and investigate the band-like, intra-flake charge transport in MXenes, we disentangled the contribution of charge mobility (μ) from carrier density (ΔN) to the photoconductivity $\Delta\sigma_{opt}$ ($= \Delta N e \mu$, where e is the elementary charge) by measuring the temperature-dependent photoconductivity spectra employing terahertz time-domain spectroscopies (THz-TDS; for details of the measurement and data analysis, see Methods). We

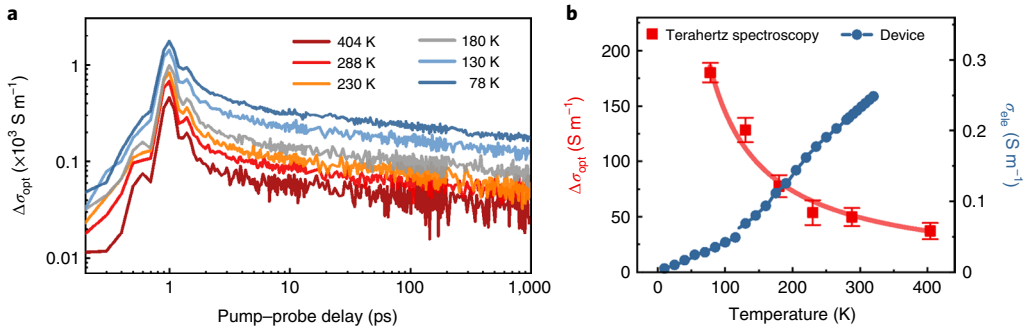

Fig. 3 | Temperature-dependent terahertz and electrical measurements for $Nb_4C_3T_x$ MXene. a, The time-resolved terahertz photoconductivity dynamics, at temperatures ranging from 78 K to 404 K under vacuum conditions (pressure of $<1.8\times10^{-4}$ mbar). The studies are conducted using excitations of 1.55 eV photons at an absorbed fluence of $\sim3.1\times10^{18}$ m^{-2}. Data are shifted horizontally by 1 ps for clarity. **b**, A direct comparison of *T*-dependent charge carrier conductivity determined optically by terahertz spectroscopy (by taking the averaged photoconductivity from 600 ps to 800 ps following excitations) and electrically via the van der Pauw four-probe method. The red line through the photoconductivity data shows a T^{-1} dependence. Error bars represent the standard error of the mean.

recorded the conductivity spectra at a delay of ~200 ps after photoexcitation to ensure a quasi-steady-state charge carrier situation. The frequency-resolved complex photoconductivity spectra are shown in Fig. 4a. We analysed the spectra using the Drude–Smith (DS) model and found that the model describes the data well. The DS model describes the transport behaviour of free carriers in a medium, where charges experience a preferentially backscattering effect due to nanoscale confinements (the presence of grain boundaries, for example)[17,27,28]. The DS model equation reads

$$\sigma(\omega) = \frac{\varepsilon_0\omega_p^2\tau}{1-i\omega\tau}\left(1+\frac{c}{1-i\omega\tau}\right),\ \text{with}\ \omega_p^2 = \frac{e^2N}{\varepsilon_0 m^*} \qquad (2)$$

where τ, ω_p, ε_0 and m^* are the effective carrier momentum scattering time, plasma frequency, vacuum permittivity and charge effective mass, respectively. The parameter c characterizes the probability that the charges backscatter between the scattering events, with the values ranging from 0 (isotropic scattering) to −1 (completely backscattering). The best fit to the DS model yields the parameters of τ, ω_p and c, which are plotted as a function of temperature (Fig. 4b and Supplementary Fig. 10). Interestingly, we find that ω_p and c depend very weakly on temperature, whereas τ increases drastically with lowering temperatures, from 38 ± 6 fs at 404 K to 95 ± 3 fs at 78 K. This substantial change demonstrates the dominant role of scattering time τ and thus effective charge mobility $\mu\ (=\frac{e\tau}{m^*}(1+c))$ (refs. [17,27]) in the d.c. limit in governing the photoconductivity amplitude as shown in Fig. 2. The threefold increase in scattering time is quantitatively consistent with the approximately three- to fourfold increase in photoconductivity amplitude. Based on these parameters, the intra-flake charge carrier mobility in $Nb_4C_3T_x$ can readily reach ~10^3 cm^2 V^{-1} s^{-1} at room temperature, using a reduced effective carrier mass of $0.04m_0$ (ref. [16]).

To quantitatively analyse the *T*-dependent scattering mechanism, we consider charge scattering contributions from both phonons and impurities following Matthiessen's Law (for an extended discussion see Methods)[25]:

$$\gamma(T) = \gamma_{ac}(T) + \gamma_{LO}(T) + \gamma_{imp}(T) \qquad (3)$$

where γ is the total scattering rate, and γ_{ac}, γ_{LO} and γ_{imp} are the scattering rates due to acoustic phonons, LO phonons and impurities, respectively.

Under the effective mass approximation, the acoustic phonon scattering rate reads[29]

$$\gamma_{ac}(T) = \frac{3m^{*3/2}E_{def}^2(k_BT)^{3/2}}{2(2\pi)^{1/2}c_{ii}\hbar^4} \qquad (4)$$

where k_B, c_{ii} and E_{def} represent the Boltzmann constant, the elastic constant and the electron deformation potential, respectively (see Methods for more details).

The term $\gamma_{LO}(T)$ describes the scattering from LO phonons following[30]

$$\gamma_{LO}(T) = \left(\frac{m_p}{m^*}\right)^2\frac{2\alpha\omega_{LO}e^{-\hbar\omega_{LO}/k_BT}}{f(\alpha)} \qquad (5)$$

where ω_{LO}, m_p and α are the angular frequency of the LO phonon, the polaron effective mass and the carrier–LO phonon coupling constant, respectively. This expression is valid in the limit of weak electron–LO phonon coupling ($\alpha<6$, justified below). $f(\alpha)$ is a dimensionless function, slowly varying from 1.0 to 1.2 for sufficiently small coupling constant ($0<\alpha<4$)[30]. Here we use $\omega_{LO}=19.5$ THz, estimated from other MXene systems[9,31,32]. This ~20-THz LO phonon mode is associated with the in-plane vibration in the carbon-based MXene structures, which is theoretically predicted to dominate the carrier–LO phonon interaction over all other phonon modes[9,33]. The calculated phonon linewidth (which is positively correlated with the electron–phonon coupling strength) for ω_{LO} (=19.5 THz) is several times higher than those for other optical phonon branches.

In contrast to the phonon-scattering mechanism, defect scattering, for example, from ionic impurities, increases as the temperature decreases. The typical temperature dependence for ionic impurity scattering rate scales as[25]

$$\gamma_{imp}(T) = A\times T^{-3/2} \qquad (6)$$

where A is a prefactor characterizing the strength of impurity scattering.

Following the above model (equations (3)–(6)), we reproduce the temperature dependence of the effective scattering rate (defined by $\gamma=\frac{1}{\tau}$) using only two adjustable parameters (A and α) (for details see Methods). As shown in Fig. 4c, the LO-phonon scattering dominates the charge transport over the entire temperature range, while impurity scattering becomes notable only at lower temperatures ($T<150$ K). Acoustic phonon scattering is not required to describe the data. This is in line with both density functional

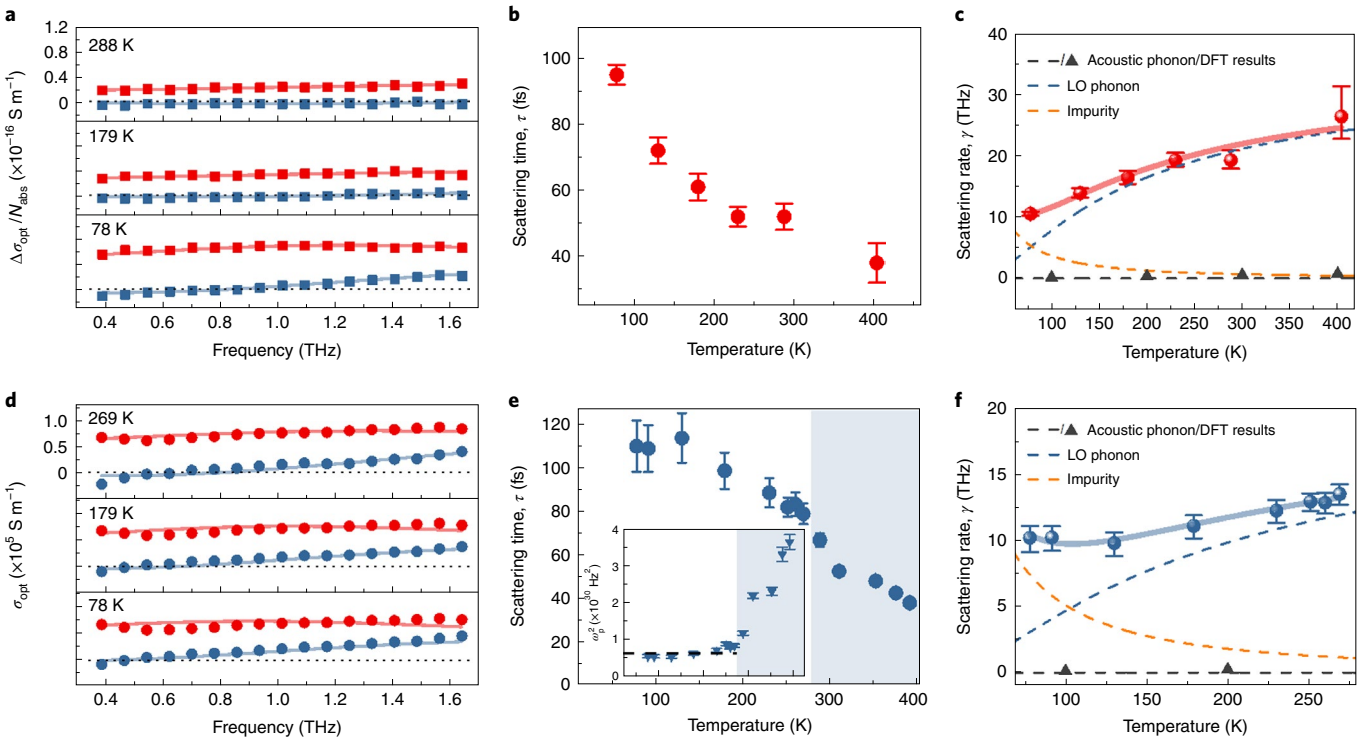

Fig. 4 | Terahertz conductivity spectra and inferred scattering time for semiconducting and metallic MXenes. a, Complex photoconductivity for the semiconductor-like $Nb_4C_3T_x$ thin film, measured at ~200 ps after photoexcitation at varying temperatures. **b**, Scattering times τ of $Nb_4C_3T_x$ as a function of temperature. **c**, *T*-dependent scattering rate of $Nb_4C_3T_x$. **d**, Complex static terahertz conductivity (σ_{opt}) for metallic $Ti_3C_2T_x$ thin films at varying temperatures. **e**, *T*-dependent scattering time of $Ti_3C_2T_x$. Inset: ω_p^2 at various *T*. The dashed lines serve as a guide to the eye. **f**, *T*-dependent scattering rate of $Ti_3C_2T_x$. In **a** and **d**, the real and imaginary parts of conductivity are shown in red and blue, respectively, and the solid lines represent the fits to the DS model explained in the main text. In **c** and **f**, the solid lines are results of a transport model that includes the acoustic phonon (black dashed line), the LO phonon (blue dashed line) and impurity scattering (orange dashed line), as described in the main text. The error bars in **b**, **c**, **e** and **f** are the standard deviations calculated from the fits. Triangles represent the carrier–acoustic phonon scattering rates obtained from the DFT calculations described in the text.

theory (DFT) calculations, which show $\gamma_{ac}(T) < 1$ THz (see below and Supplementary Fig. 15), and previous theoretical predictions[9]. The analysis yields the value of α to be 0.77 ± 0.10. The small value of α (<6) indicates the formation of large polarons in $Nb_4C_3T_x$ thin films.

The large polaron limit is further confirmed by the more general Feynman polaron theory. This theory is non-perturbative and applicable for arbitrary coupling strength[34–36]. By variationally solving the Feynman polaron model[36], the data analysis provides the carrier–LO phonon coupling constant in the range of $0.5 < \alpha < 4$ for $Nb_4C_3T_x$ (Supplementary Fig. 14a and Supplementary Discussion).

An independent estimate of the electron–phonon coupling strength can be obtained from the Landau–Pekar model (equation (7)), which is widely employed to estimate the charge–LO phonon coupling strengths[12,13,36]. Strictly speaking, the model possesses an intrinsic limitation, as it is designed to treat continuum Fröhlich polarons, but formally justified results can only be obtained in the strong electron–phonon coupling regime[13,34,37,38]:

$$\alpha = \frac{e^2}{4\pi\hbar}\frac{1}{\varepsilon_0}\left(\frac{1}{\varepsilon_{opt}} - \frac{1}{\varepsilon_s}\right)\left(\frac{m^*}{2\hbar\omega_{LO}}\right)^{1/2} \quad (7)$$

where ε_{opt} and ε_s are, respectively, the optical and static dielectric constants, and $\hbar$ is the reduced Planck constant. The dielectric function for $Nb_4C_3T_x$ MXene versus the photon energy in the infrared to ultraviolet (IR–UV) range (0.4–3.1 eV) is shown in Supplementary Fig. 11. In the measured range, our spectra are very similar to the theoretical results of that in $Ti_3C_2T_x$ MXene[39]. Therefore, considering equation (7) as well as the dielectric properties ($\varepsilon_{opt} \approx 4$–6 from our measurement, $\varepsilon_s = 22$ based on the theoretical study), we infer $0.74 < \alpha < 1.29$. This quantitative agreement between α obtained from the experiment and that obtained from the Fröhlich polaron theory supports the occurrence of large polaron transport in $Nb_4C_3T_x$ MXene materials.

Additional evidence for the dominating role of optical phonons in limiting the electrical transport properties of MXenes is provided by first-principles DFT calculations (for details see Methods). In short, we have performed numerical simulations of the full Boltzmann transport equation on Nb_4C_3, $Nb_4C_3T_x$ (with $T_x = O_2$ and $(OH)_2$), Ti_3C_2 and $Ti_3C_2T_x$ (with $T_x = (OH)_2$), using a constant relaxation time for acoustic phonons that is calculated ab initio in the deformation potential approximation. The calculated scattering rates vary with both the nature of the metal ion (being systematically smaller for Ti than for Nb) and of the functional groups (with a reduction when oxygenated species are present), but are consistently below 1 THz for all cases in the *T* range considered (Supplementary Fig. 15). This supports our claim of the minor role of acoustic phonon scattering in determining the electrical conductivity in MXenes. Furthermore, if we apply the same formalism but using the measured scattering rates (thus accounting for optical phonons), the charge mobility values at room temperature decrease from ~10^4 $cm^2 V^{-1} s^{-1}$ in the acoustic limit down to ~10^3 $cm^2 V^{-1} s^{-1}$, in good agreement with the experimental data (Supplementary Fig. 16).

Given the very similar dielectric constants for different types of MXene structure[39], we expect that the formation of large polarons in MXenes is universal. To validate such a statement, we further studied the charge transport mechanism in metallic $Ti_3C_2T_x$—the model

MXene widely used for electrochemical energy storage applications[1–3]. The metallic nature of $Ti_3C_2T_x$ MXene allows us to evaluate its complex conductivity by performing static THz-TDS measurements without involving optical excitations. In static THz-TDS measurements, we compared the amplitude and phase of the terahertz pulses transmitted through the substrate alone and the sample on the substrate in the frequency domain[17,22]. We conducted T-dependent static THz-TDS measurement from 78 to 397 K (Fig. 4d). Analysing the complex terahertz conductivity with the DS model yields scattering time τ, plasma frequency ω_p and backscattering rate c, at various T. As shown in Fig. 4e, at elevated temperatures, scattering by phonons limits the scattering time, revealing a band-like charge transport nature. Interestingly, with rising T, the ω_p^2 ($\propto$ carrier density) increases, probably due to the de-trapping of charge carriers by thermal activation (Fig. 4e, inset). The excess carrier density in the high-T regime (>288 K) could impose the additional carrier–carrier interaction channel onto the scattering mechanism. This is also supported by the T-dependent backscattering rate c, where c remains constant from 78 to 269 K, but increases in absolute magnitude when T exceeds 288 K (Supplementary Fig. 12). As such, to prevent the contribution from carrier–carrier scattering, we limited our analysis of the scattering rate in $Ti_3C_2T_x$ MXene to T ranging from 78 to 269 K. Following Matthiessen's rule and the model discussed for $Nb_4C_3T_x$, we find that the T-dependent scattering rate can be described properly by considering the scattering from phonons and impurity (for details see the Methods). As shown in Fig. 4f, the carrier–LO phonon scattering dominates the overall scattering rate in the high-T regime (>100 K), whereas the impurity scattering governs in the low-T range. Notably, the analysis yields carrier–LO phonon coupling α of 0.50 ± 0.05, indicating the formation of large polarons also in $Ti_3C_2T_x$ MXene. Independently, we further calculated α following the Landau–Pekar polaron model (equation (7)) to be between 0.44 and 1.04, and, by solving the Feynman polaron model (Supplementary Fig. 14b), we obtained the carrier–LO phonon coupling constant in the range of $0.5 < \alpha < 3$ for $Ti_3C_2T_x$. Interestingly, the inferred carrier-impurity scattering rates in both $Ti_3C_2T_x$ and $Nb_4C_3T_x$ MXenes are very similar (Supplementary Fig. 13). We observed variations in trapping due to varying defect densities in different samples, yet the charge scattering time in $Nb_4C_3T_x$ is independent of the defect level (Supplementary Fig. 9). These results suggest that charge carriers might be protected as large polarons, leading to the reduced charge scattering, despite the unavoidable high defect density in MXenes[40,41]. We note that angle-resolved photoemission spectroscopy (ARPES) is instructive for identifying the presence of polaronic features[42,43]. A recent ARPES study has provided the evidence of polaron states in single crystals of the parent phase of MXene, MAX compounds, consistent with our claim of polaron formation in MXenes[44].

Considering Fröhlich polaron theory and the similar dielectric constants for different types of MXene structure, weak carrier–LO phonon coupling is probably a generic property of MXenes, leading to large polaron formation. Experimentally, we indicate the presence of large polarons in two popular MXenes, including semiconducting $Nb_4C_3T_x$ and metallic $Ti_3C_2T_x$ MXenes. Large polaron formation may determine not only the intrinsic charge transport, but also carrier lifetimes in MXenes. For example, in organic–inorganic perovskites, the formation of large polarons has been proposed to effectively screen the defect potential, resulting in mobile charge carriers with high defect tolerance[40]. The indication of large polaron formation in MXenes may partially rationalize the reported extremely high carrier mobility in this class of 2D materials, despite structural and surface defects.

Conclusions

In this Article, we reconcile the debate between previous theoretical and experimental studies on the charge transport mechanism and propose a unifying picture of charge transport in MXenes. This is achieved by combining terahertz and static electrical transport measurements to distinguish the short- and long-range transport characteristics. We reveal that the band-like charge transport governs intra-flake charge transport in MXenes, whereas inter-flake transport occurs by hopping and becomes the limiting step for charge percolation through the network of MXene flakes. Furthermore, by analysing the charge carrier scattering following Matthiessen's law, we find that carrier–LO phonon scattering dominates the intra-flake carrier transport for both semiconducting and metallic MXenes. The resultant small carrier–LO coupling constant ($\alpha \approx 1$) indicates large polaron formation in MXenes. Our work sheds light on the polaronic nature of free charges in MXenes, and unveils intra- and inter-flake transport mechanisms in the MXene network, relevant for both fundamental studies and applications.

Online content

Any methods, additional references, Nature Research reporting summaries, source data, extended data, supplementary information, acknowledgements, peer review information; details of author contributions and competing interests; and statements of data and code availability are available at https://doi.org/10.1038/s41567-022-01541-y.

Received: 8 September 2021; Accepted: 8 February 2022;
Published online: 21 March 2022

References

1. VahidMohammadi, A., Rosen, J. & Gogotsi, Y. The world of two-dimensional carbides and nitrides (MXenes). *Science* **372**, eabf1581 (2021).
2. Jiang, X. et al. Two-dimensional MXenes: from morphological to optical, electric and magnetic properties and applications. *Phys. Rep.* **848**, 1–58 (2020).
3. Hantanasirisakul, K. & Gogotsi, Y. Electronic and optical properties of 2D transition metal carbides and nitrides (MXenes). *Adv. Mater.* **30**, 1804779 (2018).
4. Kamysbayev, V. et al. Covalent surface modifications and superconductivity of two-dimensional metal carbide MXenes. *Science* **369**, 979–983 (2020).
5. Han, M. et al. Tailoring electronic and optical properties of MXenes through forming solid solutions. *J. Am. Chem. Soc.* **142**, 19110–19118 (2020).
6. Lipatov, A. et al. Electrical and elastic properties of individual single-layer $Nb_4C_3T_x$ MXene flakes. *Adv. Electron. Mater.* **6**, 1901382 (2020).
7. Halim, J. et al. Variable range hopping and thermally activated transport in molybdenum-based MXenes. *Phys. Rev. B* **98**, 104202 (2018).
8. Hart, J. L. et al. Control of MXenes' electronic properties through termination and intercalation. *Nat. Commun.* **10**, 522 (2019).
9. Jing, Z. et al. Electron–phonon scattering limited intrinsic electrical conductivity of MXenes X_2C (X = Ti or Mo). *J. Phys. D* **54**, 015301 (2021).
10. Xu, M., Yang, J. & Liu, L. Temperaÿture-dependent optical and electrical properties of bulk Ti_2AlC and two-dimensional MXenes from first-principles. *Physica B* **560**, 146–154 (2019).
11. Zhang, X., Zhao, X., Wu, D., Jing, Y. & Zhou, Z. High and anisotropic carrier mobility in experimentally possible Ti_2CO_2 (MXene) monolayers and nanoribbons. *Nanoscale* **7**, 16020–16025 (2015).
12. Alexandrov, A. S. & Devreese, J. T. *Advances in Polaron Physics* (Springer, 2010).
13. Franchini, C., Reticcioli, M., Setvin, M. & Diebold, U. Polarons in materials. *Nat. Rev. Mater.* **6**, 560–586 (2021).
14. Mei, Y. et al. Crossover from band-like to thermally activated charge transport in organic transistors due to strain-induced traps. *Proc. Natl Acad. Sci. USA* **114**, 6739–6748 (2017).
15. Djire, A., Zhang, H., Liu, J., Miller, E. M. & Neale, N. R. Electrocatalytic and optoelectronic characteristics of the two-dimensional titanium nitride $Ti_4N_3T_x$ MXene. *ACS Appl. Mater. Interfaces* **11**, 11812–11823 (2019).
16. Shao, Y., Zhang, F., Shi, X. & Pan, H. N-functionalized MXenes: ultrahigh carrier mobility and multifunctional properties. *Phys. Chem. Chem. Phys.* **19**, 28710–28717 (2017).
17. Ulbricht, R., Hendry, E., Shan, J., Heinz, T. F. & Bonn, M. Carrier dynamics in semiconductors studied with time-resolved terahertz spectroscopy. *Rev. Mod. Phys.* **83**, 543–586 (2011).
18. Tielrooij, K. J. et al. Photoexcitation cascade and multiple hot-carrier generation in graphene. *Nat. Phys.* **9**, 248–252 (2013).
19. Fu, S. et al. Long-lived charge separation following pump-wavelength-dependent ultrafast charge transfer in graphene/WS_2 heterostructures. *Sci. Adv.* **7**, eabd9061 (2021).

20. Zheng, W., Bonn, M. & Wang, H. I. Photoconductivity multiplication in semiconducting few-layers $MoTe_2$. *Nano Lett.* **20**, 5807–5813 (2020).
21. Shan, J., Wang, F., Knoesel, E., Bonn, M. & Heinz, T. F. Measurement of the frequency-dependent conductivity in sapphire. *Phys. Rev. Lett.* **90**, 247401 (2003).
22. Němec, H., Kužel, P. & Sundström, V. Charge transport in nanostructured materials for solar energy conversion studied by time-resolved terahertz spectroscopy. *J. Photochem. Photobiol. A* **215**, 123–139 (2010).
23. Ballabio, M., Fuertes Marron, D., Barreau, N., Bonn, M. & Canovas, E. Composition-dependent passivation efficiency at the $CdS/CuIn_{1-x}Ga_xSe_2$ interface. *Adv. Mater.* **32**, 1907763 (2020).
24. Li, G. et al. Dynamÿical control over terahertz electromagnetic interference shielding with 2D $Ti_3C_2T_y$ MXene by ultrafast optical pulses. *Nano Lett.* **20**, 636–643 (2020).
25. Jacoboni, C. *Theory of Electron Transport in Semiconductors* (Springer, 2010).
26. Ippolito, S. et al. Covalently interconnected transition metal dichalcogenide networks via defect engineering for high-performance electronic devices. *Nat. Nanotechnol.* **16**, 592–598 (2021).
27. Cocker, T. L. et al. Microscopic origin of the Drude-Smith model. *Phys. Rev. B* **96**, 205439 (2017).
28. Li, G., Natu, V., Shi, T., Barsoum, M. W. & Titova, L. V. Two-dimensional MXenes $Mo_2Ti_2C_3T_z$ and $Mo_2TiC_2T_z$: microscopic conductivity and dynamics of photoexcited carriers. *ACS Appl. Energy Mater.* **3**, 1530–1539 (2020).
29. Bardeen, J. & Shockley, W. Deformation potentials and mobilities in non-polar crystals. *Phys. Rev.* **80**, 72–80 (1950).
30. Low, F. E. & Pines, D. Mobility of slow electrons in polar crystals. *Phys. Rev.* **98**, 414–418 (1955).
31. Bafekry, A., Akgenc, B., Ghergherehchi, M. & Peeters, F. M. Strain and electric field tuning of semi-metallic character $WCrCO_2$ MXenes with dual narrow band gap. *J. Phys. Condens. Matter* **32**, 355504 (2020).
32. Luo, Y., Cheng, C., Chen, H. J., Liu, K. & Zhou, X. L. Systematic investigations of the electron, phonon and elastic properties of monolayer M_2C (M = V, Nb, Ta) by first-principles calculations. *J. Phys. Condens. Matter* **31**, 405703 (2019).
33. Hu, T. et al. Vibrational properties of Ti_3C_2 and $Ti_3C_2T_2$ (T = O, F, OH) monosheets by first-principles calculations: a comparative study. *Phys. Chem. Chem. Phys.* **17**, 9997–10003 (2015).
34. Feynman, R. P., Hellwarth, R. W., Iddings, C. K. & Platzman, P. M. Mobility of slow electrons in a polar crystal. *Phys. Rev.* **127**, 1004–1017 (1962).
35. Hendry, E., Wang, F., Shan, J., Heinz, T. F. & Bonn, M. Electron transport in TiO_2 probed by THz time-domain spectroscopy. *Phys. Rev. B* **69**, 081101 (2004).
36. Frost, J. M. Calculating polaron mobility in halide perovskites. *Phys. Rev. B* **96**, 195202 (2017).
37. Sio, W. H., Verdi, C., Poncé, S. & Giustino, F. Ab initio theory of polarons: formalism and applications. *Phys. Rev. B* **99**, 235139 (2019).
38. Sio, W. H., Verdi, C., Ponce, S. & Giustino, F. Polarons from first principles, without supercells. *Phys. Rev. Lett.* **122**, 246403 (2019).
39. Berdiyorov, G. R. Optical properties of functionalized $Ti_3C_2T_2$ (T = F, O, OH) MXene: first-principles calculations. *AIP Adv.* **6**, 055105 (2016).
40. Zhu, H. et al. Screening in crystalline liquids protects energetic carriers in hybrid perovskites. *Science* **353**, 1409–1413 (2016).
41. Zhang, H. et al. Highly mobile large polarons in black phase $CsPbI_3$. *ACS Energy Lett.* **6**, 568–573 (2021).
42. Giustino, F. Electron-phonon interactions from first principles. *Rev. Mod. Phys.* **89**, 015003 (2017).
43. Wang, Z. et al. Tailoring the nature and strength of electron–phonon interactions in the $SrTiO_3$ (001) 2D electron liquid. *Nat. Mater.* **15**, 835–839 (2016).
44. Ito, T. et al. Electronic structure of Cr_2AlC as observed by angle-resolved photoemission spectroscopy. *Phys. Rev. B* **96**, 195168 (2017).

Methods

Material preparation. $Nb_4C_3T_x$ MXene was synthesized according to the previously reported hydrogen fluoride etching method[45]. Briefly, 0.8 g of Nb_4AlC_3 MAX was etched by 20 ml of 49 wt% hydrogen fluoride aqueous solution at room temperature for 96 h. After washing by deionized water until the pH was above 6.0, the obtained multilayer $Nb_4C_3T_x$ was further delaminated by tetramethylammonium hydroxide (TMAOH; 25% in H_2O) with magnetic stirring for 5 h. The $Nb_4C_3T_x$ MXene nanosheets were obtained by repeatedly washing and sonication in deionized water for 1 h. The sediment without delamination was removed by centrifugation at 2,000 r.p.m. for 20 min and the delaminated MXene flakes in supernatant were collected for subsequent measurements.

Material characterizations. The morphology of each sample was characterized via scanning electron microscopy (Zeiss Gemini S4 500) and TEM (FEI Talos F200X, 200 kV). Chemical compositions of the samples were analysed by XRD using a PW1820 X-ray diffractometer with Cu Kα radiation. Raman spectra were measured on a Renishaw inVia reflex spectrometer with a laser excitation of 532 nm. XPS spectra were recorded with a a Kratos Axis Ultra^{DLD} spectrometer using the monochromatic Al Kα source (1,486.6 eV). The static electrical conductivities were measured using the van der Pauw four-probe method, based on a commercial Lakeshore Hall system (9700A).

Terahertz spectroscopy set-up. The terahertz spectroscopy was powered by a femtosecond laser source providing pulses with a duration of ~50 fs and a repeating frequency of 1 kHz, at a central wavelength of 800 nm. The terahertz radiation was generated by the optical rectification effect in a ZnTe nonlinear crystal (along ⟨110⟩ orientation), and the terahertz probe field was mapped out through electro-optical sampling by femtosecond laser pulses in a second ZnTe detection crystal. For optical-pump terahertz probe measurements, the terahertz absorption induced by optical excitations (here, 800 nm) was monitored by fixing the sampling beam to the peak of the terahertz field. In this configuration, we measured time-dependent pump-induced terahertz absorption by tuning the time delay between the pump and terahertz probe. The entire terahertz set-up was kept under nitrogen purging to avoid terahertz absorption by vapours. The samples were either purged by dry N_2 or placed under vacuum conditions ($<2\times10^{-4}$ mbar) during measurements.

Modelling the charge scattering rate in MXenes. The charge scattering contributions were analysed following Matthiessen's law, by considering the carrier interaction with acoustic phonons, LO phonons and impurities (equation (3)). We considered the carrier–acoustic phonon scattering under the effective mass approximation (equation (4))[29], and we took the elastic constant $c_{ii}=3.86\times10^{12}$ dyn cm^{-2} from $Nb_4C_3T_x$ MXene in the literature[6]. The electron deformation potential, E_{def}, defined as the linear displacement coefficient of the single electron band energy, was used to characterize the electron–acoustic phonon coupling strength. Neither m^* nor E_{def} has been reported previously in $Nb_4C_3T_x$ MXene materials. Considering the similarity of the chemical structures of $Nb_4C_3T_x$ and Nb_2CT_x MXenes, we estimated the values of m^* and E_{def} from those in Nb_2CT_x MXene[16,46]. The modification of the lower oxidation state in the inner transition metal atoms to m^* and E_{def} is expected to be small[47–49]. For carrier–LO phonon scattering rate $\gamma_{LO}(T)$ (equation (5)), in the moderate coupling regime ($\alpha<6$) we took into account the polaron mass m_p and the effective charge mass m^* by $\frac{m_p}{m^*}=\left(1+\frac{\alpha}{6}+\frac{\alpha^2}{40}+\cdots\right)$ (ref. [30]). As for carrier-impurity scattering (equation (6)), we primarily considered the contribution from ionic impurity scattering, where the scattering increases as the temperature decreases. For modelling the scattering rate in $Ti_3C_2T_x$ MXene, we applied the same method and took the values of c_{ii}, m^* and E_{def} from the literature[46,50,51].

Computational details. DFT calculations were performed with the projector-augmented wave (PAW) basis set, as implemented in the VASP code[52,53], with the exchange and correlation effects treated at the Perdew–Burke–Ernzerhof (PBE) level[54]. Dispersion forces by Grimme correction (PBE+D2)[55] and dipole moment correction along the c axis (z direction and perpendicular to the MXene surface) were incorporated with a kinetic energy cutoff of 500 eV and using a Monkhorst–Pack sampling of $3\times3\times1$ for the Brillouin zone integration for all geometry optimizations. Vacuum spacing was set to be 30 Å to avoid the interaction with periodic images. Subsequent self-consistent field calculations were performed using a dense K-point grid of $100\times100\times1$ for the Brillouin zone integration. Electron conductivities and mobilities were estimated using the semi-classical Boltzmann transport theory within both the deformation potential approach and the relaxation time approximations[56–58].

Data availability

All data generated or analysed in this study are available from the corresponding authors upon reasonable request. Source data are provided with this paper.

Code availability

The code used to analyse the data and perform numerical simulations is available from the corresponding authors upon reasonable request.

References

45. Zhao, S. et al. Flexible $Nb_4C_3T_x$ film with large interlayer spacing for high-performance supercapacitors. *Adv. Funct. Mater.* **30**, 2000815 (2020).
46. Bai, X. et al. Two-dimensional semiconducting Lu_2CT_2 (T = F, OH) MXene with low work function and high carrier mobility. *Nanoscale* **12**, 3795–3802 (2020).
47. Yang, Y. et al. Distinguishing electronic contributions of surface and sub-surface transition metal atoms in Ti-based MXenes. *2D Mater.* **7**, 025015 (2020).
48. Zha, X. H. et al. Promising electron mobility and high thermal conductivity in Sc_2CT_2 (T = F, OH) MXenes. *Nanoscale* **8**, 6110–6117 (2016).
49. Luo, K. et al. First-principles study on the electrical and thermal properties of the semiconducting $Sc_3(CN)F_2$ MXene. *RSC Adv.* **8**, 22452–22459 (2018).
50. Lipatov, A. et al. Elastic properties of 2D $Ti_3C_2T_x$ MXene monolayers and bilayers. *Sci. Adv.* **4**, eaat0491 (2018).
51. Hu, T. et al. Anisotropic electronic conduction in stacked two-dimensional titanium carbide. *Sci. Rep.* **5**, 16329 (2015).
52. Kresse, G. & Furthmüller, J. Efficient iterative schemes for ab initio total-energy calculations using a plane-wave basis set. *Phys. Rev. B* **54**, 11169 (1996).
53. Kresse, G., Marsman, M. & Furthmüller, J. VASP (2012); https://www.vasp.at/
54. Perdew, J. P., Burke, K. & Ernzerhof, M. Generalized gradient approximation made simple. *Phys. Rev. Lett.* **77**, 3865–3868 (1996).
55. Grimme, S. Semiempirical GGA-type density functional constructed with a long-range dispersion correction. *J. Comput. Chem.* **27**, 1787–1799 (2006).
56. Madsen, G. K. H. & Singh, D. J. BoltzTraP. A code for calculating band-structure dependent quantities. *Comput. Phys. Commun.* **175**, 67–71 (2006).
57. Xi, J., Long, M., Tang, L., Wang, D. & Shuai, Z. First-principles prediction of charge mobility in carbon and organic nanomaterials. *Nanoscale* **4**, 4348–4369 (2012).
58. Slassi, A. et al. Interlayer bonding in two-dimensional materials: the special case of SnP_3 and GeP_3. *J. Phys. Chem. Lett.* **11**, 4503–4510 (2020).

Acknowledgements

Financial support by the Max Planck Society is acknowledged. This work was financially supported by the European Union's Horizon 2020 research and innovation programme (GrapheneCore3 881603) and Deutsche Forschungsgemeinschaft (MX-OSMOPED project and CRC 1415 (grant no. 417590517)). The work in Mons is financially supported by FLAG-ERA JTC 2017 project MX-OSMOPED, the Belgian National Fund for Scientific Research (FRS-FNRS), the Consortium des Equipements de Calcul Intensif (CECI) under grant no. 2.5020.11 and by the Walloon Region (ZENOBE Tier-1 supercomputer, grant no. 1117545). D.B. is FNRS Research Director. We thank K. Krewer, M. Grechko, M. Ballabio, X. Jia and A. Tries for fruitful discussions. We acknowledge P. Kumar, H. Kim and R. Ulbricht for constructive comments on the manuscript. We are grateful to H. Burg and R. Berger for conducting AFM image measurements. S.F. acknowledges fellowship support from the Chinese Scholarship Council (CSC). L.D.V. acknowledges support from the EU Horizon 2020 Framework Programme (grant no. 811284).

Author contributions

H.I.W. and M.B. conceived and designed the project. W.Z. conducted the terahertz spectroscopy experiments, analysed the data and performed the modelling. Z.L. performed van der Pauw conductivity measurements. B.S. and D.L. synthesized the sample and provided basic structural characterizations, under the supervision of M.Y. and X.F. S.M.G. and D.B. performed the DFT calculations. W.Z., H.I.W. and M.B. drafted the manuscript with input from all other authors.

Funding

Open access funding provided by Max Planck Society.

Competing interests

The authors declare no competing interests.

Additional information

Supplementary information The online version contains supplementary material available at https://doi.org/10.1038/s41567-022-01541-y.

Correspondence and requests for materials should be addressed to Hai I. Wang or Mischa Bonn.

Peer review information *Nature Physics* thanks Bing Xiao and the other, anonymous, reviewer(s) for their contribution to the peer review of this work.